On Analog Networks and Mixed-Domain Spatio-Temporal Frequency Response

Henry Man D. Ip, *Member, IEEE*, Emmanuel M. Drakakis, *Member, IEEE*, and Anil Anthony Bharath, *Member, IEEE*

***Abstract*—In this paper, we extend the linear cellular neural network (CNN) paradigm by introducing temporal derivative diffusion connections between neighboring cells. Our proposal results in an analog network topology for implementing general continuous-time discrete-space mixed-domain 3-D rational transfer functions for linear filtering. The network connections correspond one-to-one to the transfer function coefficients. The mixed-domain frequency response is treated as a temporal frequency-dependent spatial function and we show how nonseparable properties of the spatio-temporal magnitude response can be derived from the combination of: 1) sinusoidal functions of spatial frequencies and 2) polynomials of the continuous-time frequency in the 3-D frequency response expression. A generic VLSI-compatible implementation of the network based on continuous-time integrators is also proposed. Based on our proposed CNN extension, the analysis of a spatio-temporal filtering example originated from analytical modeling of receptive fields of the visual cortex is presented and a spatio-temporal cone filter is designed and presented with numerical simulation results.**

***Index Terms*—Analog signal processing, cellular neural networks (CNNs), multidimensional recursive filters, spatio-temporal filtering.**

I. Introduction

UTILIZING parallel computations from a vast amount of interconnected processing units, biological systems provide robust signal processing capabilities unmatched by conventional microelectronics. The idea of providing a high-speed, yet robust and power-efficient information processing system by using a large number of cooperating basic building blocks is exploited by engineers to build artificial neural networks aiming for various signal processing tasks. Since its introduction by Chua and Yang in 1988 [1], the cellular neural network (CNN) paradigm has established itself as one of the most efficient ways of implementing spatial filters with analog components [2]–[6]. Our work presented here focuses on analog networks for linear spatio-temporal filtering applications. An extension of the original Chua-Yang CNN (CYCNN) paradigm for linear spatio-temporal filtering was proposed in 1993 [7]: higher order temporal characteristics were imposed locally. In this paper, we further generalize the work presented in [7] to include temporal derivative coupling between cells to the original CYCNN[1] operating in its linear region [3]. This results in a network which realizes general rational nonseparable spatio-temporal transfer functions (STTFs). Furthermore, we investigate the nonseparable aspects of the filtering function in the frequency domain. It is hoped that the network formalism and the associated analysis presented here will be of use to readers that are interested in linear filtering with analog networks. 3-D spatio-temporal filtering examples with the proposed network extension are also provided.

This section revisits concisely the analysis of CNN-based linear spatial and spatio-temporal filtering operations [3], [7]. The additional temporal derivative diffusion connection to the CNN is introduced in Section II. In Section III, we analyze the resulting mixed-domain spatio-temporal frequency response as a temporal frequency-dependent spatial function. The conversion of our filtering network into spatially coupled continuous-time signal flow graphs (SFGs) suitable for VLSI implementations is detailed in Section IV, where we also contrast our formalism with multilayer CNNs (MLCNN). Finally, we provide filter analysis and synthesis examples in Section V with confirming simulation results. We conclude the paper in Section VI.

Let us first consider a simple CNN structure with each cell connected to its four immediate neighbors only [5], operating in its linear region (or equivalently, without applying the static nonlinearity at the output of each cell) and implemented by ideal operational transconductance amplifiers (OTAs). The circuit of a single cell is shown in Fig. 1, with $s(k_x, k_y)$ and $e(k_x, k_y)$ representing the output and input voltage at location (k_x, k_y), respectively. The gain (Transconductance) of each OTA is denoted as g_{mi}, for $i \in \{0, \ldots, 4\}$. This CNN has a trivial input template and a feedback cloning template given by

$$\boldsymbol{A}_T = \begin{bmatrix} 0 & g_{m4} & 0 \\ g_{m1} & -\sum_{i=0}^{4} g_{mi} & g_{m3} \\ 0 & g_{m2} & 0 \end{bmatrix}. \tag{1}$$

Applying Kirchhoff's current law (KCL) at $s(k_x, k_y)$ and assuming steady-state operation in time, and subsequently applying the 2-D z-transform with the spatial invariance assumption, yields

$$\frac{S_{z_x, z_y}}{E_{z_x, z_y}} = \frac{g_{m0}}{\sum_{i=0}^{4} g_{mi} - g_{m1} z_x^{-1} - g_{m2} z_y^{-1} - g_{m3} z_x^{+1} - g_{m4} z_y^{+1}}. \tag{2}$$

Manuscript received November 19, 2005; revised November 22, 2006, and April 12, 2007. This work was supported in part by the U.K. Research Councils under Grant GR/R87642/01. This paper was recommended by Associate Editor G. Cauwenberghs.

The authors are with the Department of Bioengineering, Imperial College London, London SW7 2AZ, U.K. (e-mail: man.ip@imperial.ac.uk; e.drakakis@imperial.ac.uk; a.bharath@imperial.ac.uk).

Digital Object Identifier 10.1109/TCSI.2007.906068

[1]Unless specified otherwise, we refer to a *single-layer* CNN structure. A discussion concerning multilayered CYCNNs is elaborated on in Section IV–B.

1549-8328/$25.00 © 2008 IEEE

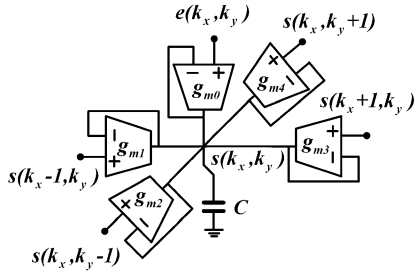


Fig. 1. Linear CNN implementation by means of transconductors.

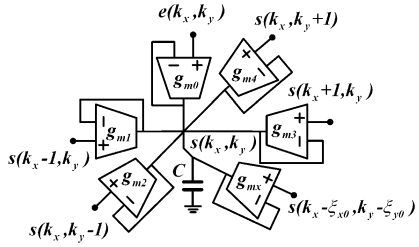


Fig. 2. "Diffusion" from node $s(k_x - \xi_{x0}, k_y - \xi_{y0})$ in a linear CNN.

The quantities z_x and z_y denote the respective spatial z-domain x and y variables, whereas S_{z_x,z_y} (i.e., $Z\{s(k_x,k_y)\}$) and E_{z_x,z_y} (i.e., $Z\{e(k_x,k_y)\}$) denote the z-transformed output and input, respectively. In general, a CNN operating in its linear region implements rational discrete spatial transfer functions [3]. This becomes clearer if we consider the "diffusion"[2] from the neighboring output node $s(k_x - \xi_{x0}, k_y - \xi_{y0})$ at relative location (ξ_{x0}, ξ_{y0}) in addition to the four neighbors in Fig. 1. The network with the additional diffusion is shown in Fig. 2. Considering the steady-state KCL after $s(k_x, k_y)$ is settled over time

$$\begin{aligned} &g_{m0}e(k_x,k_y) + g_{m1}s(k_x-1,k_y) + g_{m2}s(k_x,k_y-1) \\ &\quad + g_{m3}s(k_x+1,k_y) + g_{m4}s(k_x,k_y+1) \\ &\quad + g_{mx}s(k_x-\xi_{x0},k_y-\xi_{y0}) \\ &\qquad = \left(\sum_{i=0}^{4} g_{mi} + g_{mx}\right) s(k_x,k_y) \end{aligned} \tag{3}$$

which leads to

$$\begin{aligned} &\frac{S_{z_x,z_y}}{E_{z_x,z_y}} \\ &\quad = g_{m0} \Bigg/ \left\{ \left(\sum_{i=0}^{4} g_{mi} + g_{mx}\right) - g_{m1}z_x^{-1} - g_{m2}z_y^{-1} \right. \\ &\qquad \left. - g_{m3}z_x^{+1} - g_{m4}z_y^{+1} - g_{mx}z_x^{-\xi_{x0}}z_y^{-\xi_{y0}} \right\}. \end{aligned} \tag{4}$$

Hence, the diffusion from node $s(k_x - \xi_{x0}, k_y - \xi_{y0})$ creates terms of the form $z_x^{-\xi_{x0}} z_y^{-\xi_{y0}}$ in the denominator of the transfer function. Similarly, when "diffusing" from an additional input node $e(k_x - \xi_{x0}, k_y - \xi_{y0})$, the extra term $z_x^{-\xi_{x0}} z_y^{-\xi_{y0}}$ is created in the numerator. In other words, *the diffusion location and strength in the CNN templates are directly related to the form of the polynomials within the spatial rational transfer function of the network* [3].

Note that the above elementary analysis considers only the spatial dynamics and assumes static input with respect to time. When temporal dynamics are included (with time varying inputs/outputs as $e(k_x, k_y, t)$ and $s(k_x, k_y, t)$, respectively) and the Laplace transform is applied upon the z-transformed KCL equation at $s(k_x, k_y, t)$ in Fig. 1, we derive the following STTF:

$$\begin{aligned} \frac{S_{z_x,z_y,p_t}}{E_{z_x,z_y,p_t}} = g_{m0} \Bigg/ \Bigg\{ &\left(\sum_{i=1}^{4} g_{mi}\right) - g_{m1}z_x^{-1} - g_{m2}z_y^{-1} \\ &- g_{m3}z_x^{+1} - g_{m4}z_y^{+1} + cp_t \Bigg\}. \end{aligned} \tag{5}$$

In (5), p_t denotes the temporal Laplace variable. Under certain conditions on its coefficients, this transfer function realizes an efficient velocity selective filter [5]. In the next section, we introduce extra novel connections to linear CNNs such as the one described in Fig. 1 and show how this allows us to implement a wide range of general spatio-temporal filters.

II. Networks With Temporal Derivative Diffusion

Notice that the grounded capacitor in Figs. 1 and 2 is included in the original CNN topology [1]. How would the network dynamics change if capacitive connections existed between neighboring cells? Or more generally, how would temporal derivative diffusion from neighbors alter the spatio-temporal response properties of the network?

Consider a general lth-order derivative diffusion scheme from the general location $(k_x - \xi_{x1}, k_y - \xi_{y1})$ as shown in Fig. 3. The "derivative transconductor" $T_{x1,y1}$ (conceptually speaking) provides a current output proportional to the input voltage's lth time derivative, i.e., $i = T_{x1,y1}(d^l/dt^l)s(k_x - \xi_{x1}, k_y - \xi_{y1}, t)$. The quantity $T_{x1,y1}$ should be treated as a general coefficient of appropriate dimensions resembling the role played by a capacitor. The KCL equation at node (k_x, k_y) with voltage input and output $e(k_x, k_y, t)$ and $s(k_x, k_y, t)$, respectively, is now given by

$$\begin{aligned} &g_{m0}e(k_x,k_y,t) + g_{m1}s(k_x-1,k_y,t) \\ &\quad + g_{m2}s(k_x,k_y-1,t) + g_{m3}s(k_x+1,k_y,t) \\ &\quad + g_{m4}s(k_x,k_y+1,t) + T_{x1,y1}\frac{d^l}{dt^l}s(k_x-\xi_{x1},k_y-\xi_{y1},t) \\ &\qquad = c\dot{s}(k_x,k_y,t) + \left(\sum_{i=1}^{4} g_{mi}\right) s(k_x,k_y,t) \end{aligned} \tag{6}$$

Taking the z-transform in space and assuming spatial invariance

$$\begin{aligned} &g_{m0}E_{z_x,z_y,t} + S_{z_x,z_y,t}\left(g_{m1}z_x^{-1} + g_{m2}z_y^{-1} + g_{m3}z_x^{+1}\right. \\ &\quad \left. + g_{m4}z_y^{+1}\right) + z_x^{-\xi_{y1}}z_y^{-\xi_{y1}}T_{x1,y1}\frac{d^l}{dt^l}S_{z_x,z_y,t} \\ &\qquad = c\dot{S}_{z_x,z_y,t} + \left(\sum_{i=1}^{4} g_{mi}\right) S_{z_x,z_y,t}. \end{aligned} \tag{7}$$

[2]The term diffusion is commonly used to describe flow across a medium. Here we adopt the term to envision a directional flow of information from one node to another.

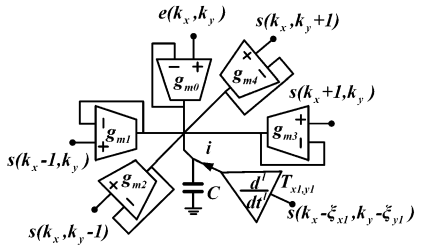


Fig. 3. CNN with temporal derivative diffusion from node $s(k_x - \xi_{x1}, k_y - \xi_{y1})$ by means of the "derivative transconductor" $T_{x1,y1}$.

Subsequently, taking the Laplace transform of (7), [7], yields

$$\begin{aligned} g_{m0}E_{z_x,z_y,p_t} + S_{z_x,z_y,p_t}\left(g_{m1}z_x^{-1} + g_{m2}z_y^{-1} + g_{m3}z_x^{+1}\right. \\ \left. + g_{m4}z_y^{+1}\right) + z_x^{-\xi_{x1}}z_y^{-\xi_{y1}}T_{x1,y1}p_t^l S_{z_x,z_y,p_t} \\ = cp_t S_{z_x,z_y,p_t} + \left(\sum_{i=1}^{4} g_{mi}\right) S_{z_x,z_y,p_t}. \end{aligned} \tag{8}$$

Rearranging (8), a STTF in the mixed temporal-Laplace/spatial-z-domain emerges

$$\begin{aligned} &\frac{S_{z_x,z_y,p_t}}{E_{z_x,z_y,p_t}} \\ &= g_{m0} \Bigg/ \left\{ g_{m0} + \sum_{i=1}^{4} g_{mi} - g_{m1}z_x^{-1} - g_{m2}z_y^{-1} - g_{m3}z_y^{+1} \right. \\ &\quad \left. - g_{m4}z_x^{+1} - T_{x1,y1}z_x^{-\xi_{x1}}z_y^{-\xi_{y1}}p_t^l + cp_t \right\}. \end{aligned} \tag{9}$$

Now it should be clear that an lth-order derivative diffusion from a general node at $(k_x - \xi_{x1}, k_y - \xi_{y1})$ creates the additional term $z_x^{-\xi_{x1}}z_y^{-\xi_{y1}}p_t^l$ in the original STTF (5). *If we diffuse the temporal derivative from an input location* $(k_x - \xi_{x1}, k_y - \xi_{y1})$, *the extra term* $z_x^{-\xi_{x1}}z_y^{-\xi_{y1}}p_t^l$ *will appear in the numerator of the transfer function. Likewise, diffusing from an output allows the extra term to be created in the denominator as in* (9). To obtain a term consisting of the Laplace variable p_t^l only, we simply have to introduce a temporal derivative diffusion from the ground node.

The above analysis reveals that *the extra temporal derivative diffusion introduced to linear CNNs, as illustrated in* Fig. 3, *enables the implementation of a general mixed-domain spatio-temporal rational transfer function in the form given below in* (10), *with a one to one correspondence of network connections and transfer function polynomial terms*

$$\frac{S_{z_x,z_y,p_t}}{E_{z_x,z_y,p_t}} = \frac{\sum_{l\in 1\ldots D}\sum_{\vec{\xi}\in B_r^2} b_l'(\vec{\xi})z_x^{\xi_x}z_y^{\xi_y}p_t^l}{\sum_{l\in 1\ldots D}\sum_{\vec{\xi}\in B_r^2} a_l'(\vec{\xi})z_x^{\xi_x}z_y^{\xi_y}p_t^l} \tag{10}$$

with $\vec{\xi} = (\xi_x, \xi_y) \in N^2$ and the region of support B_r^2 [7] defined in 2-D space as

$$B_r^2 = \{(x,y) \in N^2 | x|, |y| \le r\}. \tag{11}$$

The quantities $a_l'(\vec{\xi})$ and $b_l'(\vec{\xi})$ are in general complex constants for $l \in Z_+$, though we only consider real values in this presentation. The differential equation corresponding to (10) is given by

$$\begin{aligned} c\dot{s}(\vec{k},t) = &-\frac{1}{R}s(\vec{k},t) + \sum_{\vec{\xi}\in B_r^2} a_0(\vec{\xi})s(\vec{k}+\vec{\xi},t) \\ &+ \sum_{\vec{\xi}\in B_r^2} b_0(\vec{\xi})e(\vec{k}+\vec{\xi},t) \\ &+ \sum_{l\in 1\ldots D}\left[\sum_{\vec{\xi}\in B_r^2} a_l(\vec{\xi})\frac{d^l s(\vec{k}+\vec{\xi},t)}{dt^l}\right. \\ &\left. + \sum_{\vec{\xi}\in B_r^2} b_l(\vec{\xi})\frac{d^l e(\vec{k}+\vec{\xi},t)}{dt^l}\right] \end{aligned} \tag{12}$$

with parameters related to (10) as follows:

$$a_0'(0,0) = \frac{1}{R} - a_0(0,0), \quad \text{otherwise } a_0'(\vec{\xi}) = -a_0(\vec{\xi}) \tag{13}$$

$$a_1'(0,0) = c - a_1(0,0), \quad \text{otherwise } a_l'(\vec{\xi}) = -a_1(\vec{\xi}), \quad \text{for } l \ge 1 \tag{14}$$

$$b_l'(\vec{\xi}) = b_l(\vec{\xi}) \tag{15}$$

where R is a real constant. From the differential equation we can now define network cloning templates. Immediately we recognize that (12) without the expression in the third line corresponds to the dynamics of the original CYCNN operating in its linear region (linear CNNs). Therefore, we have CNN feedback and feedforward templates being $\boldsymbol{A} = a_0(\vec{\xi})_{\vec{\xi}\in B_r^2}$ and $\boldsymbol{B} = b_0(\vec{\xi})_{\vec{\xi}\in B_r^2}$, respectively. We can define extra cloning templates for the time-derivative terms in the third line of (12): $\boldsymbol{A}_l = a_l(\vec{\xi})_{\vec{\xi}\in B_r^2}$ and $\boldsymbol{B}_l = b_l(\vec{\xi})_{\vec{\xi}\in B_r^2}$, respectively, as the lth derivative feedback and feedforward cloning templates. *Note that each term in the differential* equation (12) *corresponds to one term in the transfer function* (10) *and also to one network connection (one coefficient in the templates). This facilitates the interpretation of the filtering function directly from the network topology*. The general STTF representing linear CNNs without the extra time derivative diffusion is given by

$$\frac{S_{z_x,z_y,p_t}}{E_{z_x,z_y,p_t}} = \frac{\sum_{\vec{\xi}\in B_r^2} b_0(\vec{\xi})z_x^{\xi_x}z_y^{\xi_y}}{\sum_{\vec{\xi}\in B_r^2} a_0(\vec{\xi})z_x^{\xi_x}z_y^{\xi_y} + cp_t}. \tag{16}$$

Comparing (10) and (16) reveals that the extra temporal derivative diffusion connections to linear CNNs enable a richer spatio-temporal characteristic to be realized.

An arbitrary stable rational STTF, either in the z- or Laplace domain, can be converted to the form described in (10) by applying the appropriate bilinear transform (or its inverse) to the spatial (given a continuous prototype) or temporal (given a discrete prototype) variable(s) [8].

Note that we do not impose any restrictions on the signs of $\vec{\xi} = (\xi_x, \xi_y)$ in (12). This corresponds to the current cell taking information from neighbors of all directions just like in the CYCNN case. From a filtering point of view, we have general support (recurring in both causal and anti-causal directions) discrete systems that are not necessarily recursible [9]. Despite

nonrecursible structures not being suitable for direct implementation on delay based digital systems, analog VLSI arrays such as the CNNUM [10] are particularly suited for the implementation of general support dynamics. Preliminary results from our ongoing research on analog VLSI implementations of the network proposed here are reported elsewhere [11]. The general support nature of CNNs results in a rather slack stability criterion that allows a greater freedom for pole locations than purely causal or purely anti-causal systems. This facilitates a convenient 3-D pole placement scheme for filter synthesis [12], which cannot be carried out for designing stable causal/anti-causal filters for delay implementation in digital systems. Specifically, we treat the denominator of (10) as a polynomial of the temporal Laplace variable p_t and solve for the poles in terms of (z_x, z_y). The condition for BIBO stability of a spatial general support and causal time network implementing (10) is given by [13]—there are no poles in the space of

$$|z_x| = 1 \cap |z_y| = 1 \cap \mathrm{Re}\{p_t\} \geq 0 \tag{17}$$

which reduces to having all poles lying on the dual unit circles to be on the left half temporal-Laplace plane.

III. Mixed-Domain Spatio-Temporal Magnitude Response

In this section, we demonstrate a way of analyzing the continuous-time/discrete-space transfer function described in the preceding section. It is hoped that the analysis presented in this section will facilitate the reader to visualize how a rational STTF behaves in the spatio-temporal frequency domain. Note that an insightful treatment on the analysis of CNN STTFs by Shi *et al.* can be found in [7]. In the case of [7], the STTF is treated as a spatial frequency-dependent temporal filter, with emphasis placed on pole locations. The analysis presented in [7] is also useful for intuitive design of spatio-temporal filters with our modified CNN. We elaborate on this in a companion paper [12]. Here we propose an alternative approach in analyzing 3-D STTFs: the general equation (10), describing STTFs realized by CNNs with the additional temporal derivative diffusion, is treated as a *temporal frequency-dependent spatial filter*. Unlike 1-D systems, a coherent phase is not well defined in 2-D and 3-D cases [14]. Hence, we focus on the magnitude response only. Furthermore, all coefficients in (10) are assumed to be real numbers. As we will see, our analysis of 3-D STTFs leads to the visualization of rather simple combinations of 2-D sinusoidal functions of the 2-D "discrete" frequencies (ω_x, ω_y), and the temporal frequency Ω_t. A similar analysis of CNN spatio-temporal filters in the time domain is presented in [3]. However, the discussion here focuses on general spatio-temporal *frequency-domain characteristics of CNNs with our proposed extra connections*. Two specific examples in Section V are analyzed with the techniques presented in this section.

Mixed-domain transfer functions in the form of (10) seem to be intuitively easier to understand than 3-D functions solely in the Laplace or z-domain. Suppose we move along the time-frequency axis Ω_t (with substitution $p_t = j\Omega_t$) and let us consider *slices of the response parallel to the spatial frequency plane* (ω_x, ω_y). i.e., treating the STTF as implementing a *temporal frequency-dependent spatial filter*. This way, space-time *nonseparable* characteristics become clear as the spatial response varies nonhomogeneously across space with temporal frequency. Looking at (10) again, at low values of Ω_t close to zero, terms without p_t dominate. The "spatial response slices" are approximated by (10) with all terms that have the p_t factor removed. As we increase Ω_t, the response will be a mix of terms with powers of p_t as their factor. As Ω_t gets larger, the response is dominated by terms incorporating the highest powers of p_t. The above observation does not apply to pure Laplace or z-domain STTFs. In the case of pure z-domain STTFs, all frequency variables are embedded in sinusoidal functions, hence it would be hard to tell which frequency variable dominates under certain conditions. For STTFs in the Laplace-domain only, it is not entirely obvious (without detailed analysis) what happens to the overall magnitude response when two or more frequency variables become very large.

We start by finding out what algebraic functions of $(\omega_x, \omega_y, \Omega_t)$ need to be investigated in order to understand the space-time nonseparable property of the magnitude response of a particular STTF. Consider a general term in (10), as part of the numerator or denominator polynomial

$$\cdots + D p_t^l z_x^{\xi_x} z_y^{\xi_y} + \cdots \tag{18}$$

where the coefficient D is a real constant. The frequency response of (18) is given by

$$\begin{aligned}\cdots &+ (-1)^{\frac{l}{2}} D\Omega_t^l \cos(\xi_x\omega_x + \xi_y\omega_y) \\ &+ j(-1)^{\frac{l}{2}} D\Omega_t^l \sin(\xi_x\omega_x + \xi_y\omega_y) + \cdots, j^2 = -1\end{aligned} \tag{19}$$

note that we only consider real coefficients in (10). Let

$$\Lambda_1 = (-1)^{\frac{l}{2}} D\Omega_t^l \cos(\xi_x\omega_x + \xi_y\omega_y) \tag{20}$$

and

$$\Lambda_2 = j(-1)^{\frac{l}{2}} D\Omega_t^l \sin(\xi_x\omega_x + \xi_y\omega_y). \tag{21}$$

Both Λ_1 and Λ_2 incorporate the factor $(-1)^{(l/2)} = j^l$. Depending on the value of the integer $l \geq 0$, one of the terms will be real and the other imaginary. Without loss of generality, we group the terms into real and imaginary expressions

$$\begin{aligned}&\left[\cdots + (-1)^{\frac{l}{2}} D\Omega_t^l \Gamma_{\xi_x,\xi_y} + \cdots\right] \\ &\quad + j\left[\cdots + (-1)^{\frac{l}{2}} D\Omega_t^l \Delta_{\xi_x,\xi_y} + \cdots\right] \\ &\quad = [\cdots + \Lambda_1 + \cdots] + j\left[\cdots + \frac{\Lambda_2}{j} + \cdots\right] \\ &\quad = K_r + jK_i\end{aligned} \tag{22}$$

where

$$\Gamma_{\xi_x,\xi_y} = \cos(\xi_x\omega_x + \xi_y\omega_y) \tag{23}$$

$$\Delta_{\xi_x,\xi_y} = \sin(\xi_x\omega_x + \xi_y\omega_y). \tag{24}$$

For the convenience of our discussion, the notations introduced by (23) and (24) are followed hereafter for expressing 2-D sinusoidal functions. When evaluating the magnitude of (22), provided that one of K_r and K_i (or Λ_1 and Λ_2) is real and the

TABLE I
COMPOSITION OF ODD/EVEN STTF FREQUENCY TERMS

Real	Imaginary
$\Omega_t^{l_n} sin(\xi_x\omega_x + \xi_y\omega_y)$	$sin(\xi_x\omega_x + \xi_y\omega_y)$
$cos(\xi_x\omega_x + \xi_y\omega_y)$	$\Omega_t^{l_m} sin(\xi_x\omega_x + \xi_y\omega_y)$
$\Omega_t^{l_m} cos(\xi_x\omega_x + \xi_y\omega_y)$	$\Omega_t^{l_n} cos(\xi_x\omega_x + \xi_y\omega_y)$
$\Omega_t^{l_m}$	$\Omega_t^{l_n}$
c_0	

other is imaginary, their true identity is not important as they will be both squared and added. What affects the response is how Λ_1 and Λ_2, respectively, interact with other terms in K_r and K_i. Assuming real coefficients, it can be verified that the respective contributions of real and imaginary parts are equal to the sum of the terms in the same corresponding columns of Table I, where l_n and l_m are, respectively, odd and even integers with c_0 being a constant.

The product terms of temporal frequency and sinusoidal functions are due to the extra temporal derivative diffusion connections. To illustrate how the powers of Ω_t combine with sinusoidal functions of the discrete frequencies (ω_x, ω_y) to produce space-time nonseparable frequency characteristics: rather than attempting to provide an exhaustive list of responses, we focus upon some commonly encountered frequency response terms appearing in both the numerator and denominator of a second-order system

$$R1(\omega_x,\omega_y,\Omega_t) = \left\{c_0 + \Omega_t\left[D_1\Delta_{\xi_{x1},\xi_{y1}} + D_2\Delta_{\xi_{x2},\xi_{y2}}\right]\right\}^2 \quad (25)$$

$$R2(\omega_x,\omega_y,\Omega_t) = \left\{c_0 + D_3\Omega_t^2 + \Omega_t[D_1\Delta_{\xi_{x1},\xi_{y1}} + D_2\Delta_{\xi_{x2},\xi_{y2}}]\right\}^2 \quad (26)$$

$$R3(\omega_x,\omega_y,\Omega_t) = \left\{c_0 + \Omega_t\left[D_1\Delta_{\xi_{x1},\xi_{y1}} + D_2\Delta_{\xi_{x2},\xi_{y2}}\right] + \Omega_t^2\left[D_3\Gamma_{\xi_{x3},\xi_{y3}} + D_4\Gamma_{\xi_{x4},\xi_{y4}}\right]\right\}^2 \quad (27)$$

$$I1(\omega_x,\omega_y,\Omega_t) = \left\{\Omega_t + D_1\Delta_{\xi_{x1},\xi_{y1}} + D_2\Delta_{\xi_{x2},\xi_{y2}}\right\}^2 \quad (28)$$

$$I2(\omega_x,\omega_y,\Omega_t) = \left\{\Omega_t + \Omega_t^2\left[D_1\Delta_{\xi_{x1},\xi_{y1}} + D_2\Delta_{\xi_{x2},\xi_{y2}}\right]\right\}^2 \quad (29)$$

$$I3(\omega_x,\omega_y,\Omega_t) = \left\{D_1\Delta_{\xi_{x1},\xi_{y1}} + D_2\Delta_{\xi_{x2},\xi_{y2}} + \Omega_t\left[D_3\Gamma_{\xi_{x3},\xi_{y3}} + D_4\Gamma_{\xi_{x4},\xi_{y4}}\right]\right\}^2 \quad (30)$$

$$I4(\omega_x,\omega_y,\Omega_t) = \left\{\Omega_t\left[D_1\Gamma_{\xi_{x1},\xi_{y1}} + D_2\Gamma_{\xi_{x2},\xi_{y2}}\right] + \Omega_t^2\left[D_3\Delta_{\xi_{x3},\xi_{y3}} + D_4\Delta_{\xi_{x4},\xi_{y4}}\right]\right\}^2 \quad (31)$$

where $\xi_{x1}\cdots\xi_{x4}$ and $\xi_{y1}\cdots\xi_{y4}$ are constant integers and $D_1\cdots D_4$ are real constants relating to the cloning templates and STTF coefficients, *which in turn relate to the location and order of the temporal-derivative and spatial diffusion network connections*. We now present the visualization of expressions $R1(\omega_x,\omega_y,\Omega_t)$ to $I4(\omega_x,\omega_y,\Omega_t)$ in (25)–(31) in order to study how these terms contribute to a space-time nonseparable

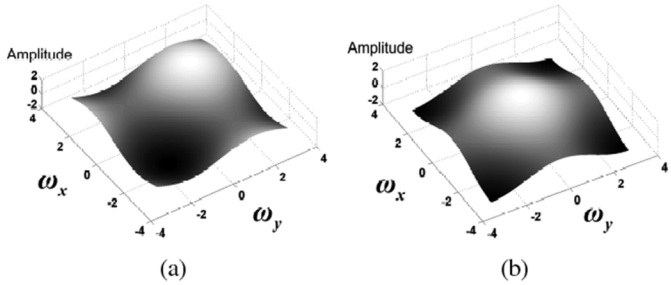


Fig. 4. Visualization of sinusoidal functions (a) $\sin(\omega_{\xi_x}) + \sin(\omega_{\xi_y})$, and (b) $\cos(\omega_{\xi_x}) + \cos(\omega_{\xi_y})$.

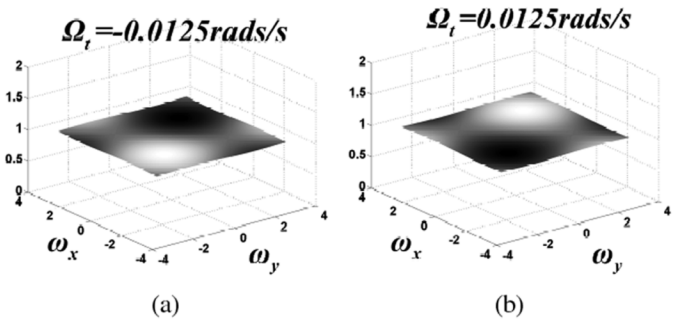


Fig. 5. Behavior of $R1(\omega_x,\omega_y,\Omega_t)$ near the origin Ω_t with $\xi_{x1} = \xi_{y2} = D_1 = D_2 = 1, c_0 = 1$, and $\xi_{y1} = \xi_{x2} = 0$.

magnitude characteristic. Convenient parameter values are chosen to facilitate the interpretation of the visualizations. As explained before, we consider slices of the magnitude expressions parallel to the plane of spatial frequency axis (ω_x,ω_y) as we move along the temporal axis Ω_t.

A. $R1(\omega_x,\omega_y,\Omega_t)$

The behavior of $R1(\omega_x,\omega_y,\Omega_t)$ near the origin is plotted in Fig. 5, which shows a shift in emphasis across the spatial domain as we move from a negative temporal frequency Ω_t to a positive temporal frequency (hence the frequency response is not space-time separable). This effect can be understood by observing that the two dimensional sine function shown in Fig. 4(a) has both positive and negative values across space. When this 2-D sine function is added to a positive constant c_0 (unity in our case), the positive sinusoidal part is emphasized, whereas the negative part is diminished. Generating $R1(\omega_x,\omega_y,\Omega_t)$ in the transfer function could create space-time nonseparable asymmetry in the magnitude response at low temporal frequencies.

B. $R2(\omega_x,\omega_y,\Omega_t)$

The behavior of $R2(\omega_x,\omega_y,\Omega_t)$ near the origin does not differ significantly from that of $R1$ in Fig. 5. This is expected as $R1(\omega_x,\omega_y,\Omega_t)$ and $R2(\omega_x,\omega_y,\Omega_t)$ only differ by a squared term of the temporal frequency. At small values of $|\Omega_t|$, the Ω_t^2 term is negligible. However, $R1(\omega_x,\omega_y,\Omega_t)$ and $R2(\omega_x,\omega_y,\Omega_t)$ have quite different "asymptotic behavior" at relatively higher values of $|\Omega_t|$. The asymmetry term $\Omega_t[D_1\Delta_{\xi_{x1},\xi_{y1}} + D_2\Delta_{\xi_{x2},\xi_{y2}}]$ dominates the symmetrical constant c_0 in $R1(\omega_x,\omega_y,\Omega_t)$ at higher values of $|\Omega_t|$. Hence, when squared, we have the two minimum/maximum lobes of the sinusoidal function in Fig. 4(a) approaching each other

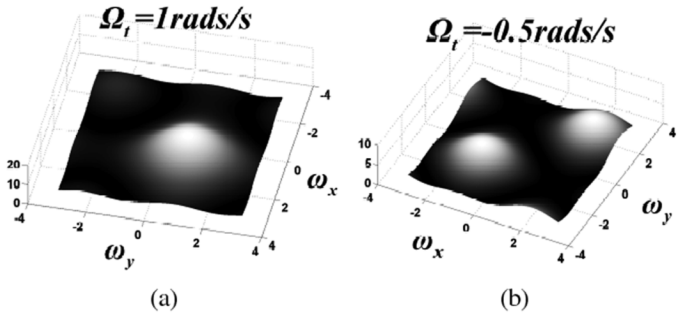


Fig. 6. (a) Behavior of $R3(\omega_x, \omega_y, \Omega_t)$ at $\Omega_t = 1$ with $\xi_{y1} = \xi_{x2} = \xi_{y3} = \xi_{x4} = 0, c_0 = 1$ and $\xi_{x1} = \xi_{y2} = \xi_{x3} = \xi_{y4} = D_1 = D_2 = D_3 = D_4 = 1$. (b) $I3(\omega_x, \omega_y, \Omega_t)$ with $\xi_{y1} = \xi_{x2} = \xi_{y3} = \xi_{x4} = 0$ and $\xi_{x1} = \xi_{y2} = \xi_{x3} = \xi_{y4} = D_1 = D_2 = D_3 = D_4 = 1$ when $\Omega_t = -0.5$ rads/s.

in magnitude. As stated above, the asymmetry of the main lobes is created by the combination of a positive constant and the spatial fluctuation of a 2-D sine function centered at zero. For $R2(\omega_x, \omega_y, \Omega_t)$, the Ω_t^2 term plays the role of the constant term in $R1(\omega_x, \omega_y, \Omega_t)$. Furthermore, unlike $R1(\omega_x, \omega_y, \Omega_t)$, in $R2(\omega_x, \omega_y, \Omega_t)$ the term Ω_t^2 is not "taken over" by $\Omega_t[D_1\Delta_{\xi_{x1},\xi_{y1}} + D_2\Delta_{\xi_{x2},\xi_{y2}}]$ at higher values of $|\Omega_t|$. Therefore, the spatial shape at low temporal frequency is preserved at higher temporal frequencies. However, at even higher values of Ω_t, the Ω_t^2 term takes over $R2(\omega_x, \omega_y, \Omega_t)$ in such a manner that the variation of magnitude over space is small compared to the mean magnitude.

C. $R3(\omega_x, \omega_y, \Omega_t)$

The expression $R3(\omega_x, \omega_y, \Omega_t)$ resembles the expression $R1(\omega_x, \omega_y, \Omega_t)$ but with the extra cosine terms. Since the cosine terms have a factor of Ω_t^2, at low frequencies $R3(\omega_x, \omega_y, \Omega_t)$ is very similar to $R1(\omega_x, \omega_y, \Omega_t)$ and $R2(\omega_x, \omega_y, \Omega_t)$. As shown in Fig. 4(b), 2-D cosine spatial functions have positive values near the origin and negative values at points in the periphery. When the cosine terms are combined with a positive constant Ω_t^2 and squared, the overall effect is to emphasize the area around the origin and diminish the periphery area. Provided that Ω_t is large enough for the Ω_t^2 term to contribute significantly to the overall function and without being too large to overwhelm the other terms; the overall result is again similar to $R1(\omega_x, \omega_y, \Omega_t)$ but with the "peaks" pushed towards the origin [Fig. 6(a)]. At higher values of $|\Omega_t|$, the Ω_t^2 term takes over in $R3(\omega_x, \omega_y, \Omega_t)$ and the cosine terms dominate.

D. $I1(\omega_x, \omega_y, \Omega_t)$

Now let us study the nonseparable effects produced by the imaginary parts. At low temporal frequency $|\Omega_t|, I1(\omega_x, \omega_y, \Omega_t)$ is dominated by the sine terms. Hence, we have two main peaks as the minimum/maximum lobes of the sinusoidal function [Fig. 4(a)] is squared. As Ω_t increases in the positive direction, the positive part of the spatial sine function is enhanced, whereas the negative part is reduced in magnitude. Likewise, if Ω_t decreases from zero, the negative part of the sine function is enhanced and the positive part is reduced. Hence, we have a reduced magnitude in either of the peaks in a squared sinusoidal function as we deviate from the origin along the Ω_t axis. Further increase in $|\Omega_t|$ renders the sine functions relatively insignificant and the fluctuation of $I1(\omega_x, \omega_y, \Omega_t)$ is small compared to its mean value.

E. $I2(\omega_x, \omega_y, \Omega_t)$

Now consider the expression for $I2(\omega_x, \omega_y, \Omega_t)$. At $|\Omega_t| = 0$, the value of $I2(\omega_x, \omega_y, \Omega_t)$ is zero. With $|\Omega_t|$ staying at a low value, the contribution from the sine functions are small as they are multiplied by Ω_t^2 and $I2(\omega_x, \omega_y, \Omega_t)$ is approximately mirrored across $|\Omega_t| = 0$. i.e., it behaves as an even function of Ω_t. As $|\Omega_t|$ increases, due to arguments similar to the analysis of $I1(\omega_x, \omega_y, \Omega_t)$, we have two main peaks, each peak taking turns to dominate depending on the sign of Ω_t. At higher values of $|\Omega_t|$, the sine term dominates $I2(\omega_x, \omega_y, \Omega_t)$ with a factor of Ω_t^2 and we have two main peaks restored.

F. $I3(\omega_x, \omega_y, \Omega_t)$

At low temporal frequency, $I3(\omega_x, \omega_y, \Omega_t)$ resembles the combination of spatial cosine and sine functions illustrated in Fig. 4(a)–(b). Two peaks are generated by the constructive combination of regions with the same polarity in the sine and cosine functions [Fig. 6(b)]. As $|\Omega_t|$ is increased, the two peaks migrate towards the origin along the diagonal direction. This is as expected: as we increase $|\Omega_t|$, the relative contribution of the cosine term increases and it has emphasis in the middle and at the corners when squared. Finally, we expect five peaks as the cosine function completely dominates the sine function when Ω_t is large, similar to the behavior of $R3(\omega_x, \omega_y, \Omega_t)$ at higher $|\Omega_t|$ values.

G. $I4(\omega_x, \omega_y, \Omega_t)$

For the range of values of $|\Omega_t|$ when Ω_t^2 is comparable to $|\Omega_t|, I4(\omega_x, \omega_y, \Omega_t)$ behaves similarly to $I3(\omega_x, \omega_y, \Omega_t)$. However, at zero temporal frequency, the expression evaluates to zero. At larger values of $|\Omega_t|, I4(\omega_x, \omega_y, \Omega_t)$ is dominated by the sine term with two main peaks.

The previous analysis concentrated upon the study of specific spatio-temporal terms that are frequently encountered in the numerator or denominator of the general STTF codified by (10). Treating the composite magnitude response as a temporal-frequency-dependent spatial filter provides insight in a systematic manner upon its subtle *nonseparable* space-time characteristics. i.e., for all the expressions (25)–(31) under consideration: as we move along the temporal frequency axis Ω_t, we observe that the spatial response varies nonhomogeneously across space. In Section V we elaborate on two specific filtering examples.

IV. VLSI-Compatible Implementations

As explained at the end of Section II, analog VLSI are particularly suited for implementing spatio-temporal filtering networks. In analog VLSI, linear signal processing operations are often realized with continuous-time integrators as a fundamental building block [15], [16]. Here we propose a transformation, based on SFG manipulation, for implementing the suggested network dynamics with spatially coupled continuous-time integrators. With the aid of the SFG, we can also examine how our proposed time-derivative diffusion connections on linear CNNs compares with the spatio-temporal dynamics realized by MLCNNs.

A. Continuous-Time SFGs

Consider the differential equation describing the network dynamics (12) and let L and D be the respective degrees of the temporal Laplace polynomials in the denominator and numerator of the transfer function. We also make the reasonable assumption of $L \geq D$. Consider the Laplace transform of (12)

$$\begin{aligned} p_t S(\vec{k},p_t) = &-\frac{1}{cR}S(\vec{k},p_t)+\frac{1}{c}\sum_{\vec{\xi}\in B_r^2} a_0(\vec{\xi})S(\vec{k}+\vec{\xi},p_t) \\ &+\frac{1}{c}\sum_{\vec{\xi}\in B_r^2} b_0(\vec{\xi})E(\vec{k}+\vec{\xi},p_t) \\ &+\sum_{l\in 1..L}\sum_{\vec{\xi}\in B_r^2} a_l(\vec{\xi})p_t^l S(\vec{k}+\vec{\xi},p_t) \\ &+\sum_{l\in 1..D}\sum_{\vec{\xi}\in B_r^2} b_l(\vec{\xi})p_t^l E(\vec{k}+\vec{\xi},p_t). \end{aligned} \tag{32}$$

Setting $A = a_L(0,0) \neq 0$ yields

$$\begin{aligned} p_t S(\vec{k},p_t) = &-\frac{1}{cR}S(\vec{k},p_t)+\frac{1}{c}\sum_{\vec{\xi}\in B_r^2} a_0(\vec{\xi})S(\vec{k}+\vec{\xi},p_t) \\ &+\frac{1}{c}\sum_{\vec{\xi}\in B_r^2} b_0(\vec{\xi})E(\vec{k}+\vec{\xi},p_t)+Ap_t^L S(\vec{k},p_t) \\ &+\sum_{\vec{\xi}\neq(0,0)\in B_r^2} a_L(\vec{\xi})p_t^L S(\vec{k}+\vec{\xi},p_t) \\ &+\sum_{l\in 1..L-1}\sum_{\vec{\xi}\in B_r^2} a_l(\vec{\xi})p_t^l S(\vec{k}+\vec{\xi},p_t) \\ &+\sum_{l\in 1..D}\sum_{\vec{\xi}\in B_r^2} b_l(\vec{\xi})p_t^l E(\vec{k}+\vec{\xi},p_t). \end{aligned} \tag{33}$$

In other words, we assume that at least one of the highest power p_t^L terms in the denominator is free of the z-domain variables z_x and z_y in its coefficient. This is a reasonable assumption since any terms in the form $p_t^L z_x^{-a} z_y^{-b}$ can have the z-domain variables eliminated by multiplying the whole transfer function by $z_x^{+a}z_y^{+b}/z_x^{+a}z_y^{+b}$. However, this affects the stability criterion of the filter [13]. In the case for which an unstable transfer function results after the multiplication of $z_x^{+a}z_y^{+b}/z_x^{+a}z_y^{+b}$, the filter is not suitable for the integrator-based implementation outlined here.

An integral equation in the Laplace domain can be obtained after dividing (33) by Ap_t^L and rearranging

$$\begin{aligned} S(\vec{k},p_t) = &\frac{1}{cRAp_t^L}S(\vec{k},p_t)-\frac{1}{c}\sum_{\vec{\xi}\in B_r^2}\frac{a_0(\vec{\xi})S(\vec{k}+\vec{\xi},p_t)}{Ap_t^L} \\ &-\frac{1}{c}\sum_{\vec{\xi}\in B_r^2}\frac{b_0(\vec{\xi})E(\vec{k}+\vec{\xi},p_t)}{Ap_t^L}+\frac{1}{Ap_t^{L-1}}S(\vec{k},p_t) \\ &-\sum_{l\in 1...L-1}\sum_{\vec{\xi}\in B_r^2}\frac{a_l(\vec{\xi})S(\vec{k}+\vec{\xi},p_t)}{Ap_t^{L-l}} \\ &-\sum_{l\in 1...D}\sum_{\vec{\xi}\in B_r^2}\frac{b_l(\vec{\xi})E(\vec{k}+\vec{\xi},p_t)}{Ap_t^{L-l}} \\ &-\sum_{\vec{\xi}\in B_r^2,\neq\vec{0}}\frac{a_L(\vec{\xi})S(\vec{k}+\vec{\xi},p_t)}{A}. \end{aligned} \tag{34}$$

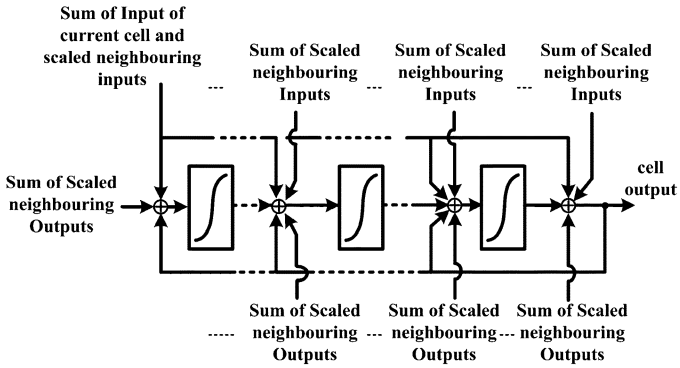


Fig. 7. Schematic of the SFG implementation of the proposed spatio-temporal filtering network. Detailed correlation between the SFG gain terms and STTF coefficients can be found in [17]. The cell output (or inputs to other integrators) is computed by the sum of the output of the last integrator and contribution from neighboring cells. In practical implementations, this would require extra circuit blocks to handle the signal summation and distribution [11].

The relation (34) governs the temporal dynamics at each cell, with input/outputs of neighboring cells as inputs to the current cell. For clarity, we use $S^{L-l}_{\vec{\xi}+\vec{k}}$ to denote the $S(\vec{\xi}+\vec{k},p_t)$ terms in (34) with a coefficient involving the term $1/p_t^{L-l}$. Similarly, for neighboring inputs that are also connected to the current cell, we have $E^{L-l}_{\vec{\xi}+\vec{k}}$. Hence, (34) becomes

$$\begin{aligned} S(\vec{k},p_t) = &\frac{1}{cRAp_t^L}S^L_{\vec{k}}-\frac{1}{c}\sum_{\vec{\xi}\in B_r^2}\frac{a_0(\vec{\xi})S^L_{\vec{k}+\vec{\xi}}}{Ap_t^L} \\ &-\frac{1}{c}\sum_{\vec{\xi}\in B_r^2}\frac{b_0(\vec{\xi})E^L_{\vec{k}+\vec{\xi}}}{Ap_t^L}+\frac{1}{Ap_t^{L-1}}S^{L-1}_{\vec{k}} \\ &-\sum_{l\in 1...L-1}\sum_{\vec{\xi}\in B_r^2}\frac{a_l(\vec{\xi})S^{L-l}_{\vec{k}+\vec{\xi}}}{Ap_t^{L-l}} \\ &-\sum_{l\in 1...D}\sum_{\vec{\xi}\in B_r^2}\frac{b_l(\vec{\xi})E^{L-l}_{\vec{k}+\vec{\xi}}}{Ap_t^{L-l}}-\sum_{\vec{\xi}\in B_r^2,\neq\vec{0}}\frac{a_L(\vec{\xi})S_{\vec{k}+\vec{\xi}}}{A}. \end{aligned} \tag{35}$$

We can now construct a SFG from (35), *based on integrators only*. A simplified SFG omitting for the sake of clarity the detailed "gain terms" is shown in Fig. 7. The input of the integrators originates not just from the current cell's input/output but also the input/output of neighboring cells. Therefore, the SFG of our modified CNN presented here is spatially coupled. Note that the SFG presented in Fig. 7 is general. For any $s^{L-l}_{\vec{k}+\vec{\xi}}$ with $\vec{\xi}=\vec{0}$, we have local feedback in the SFG. Also, if there exist terms in the form of $s^{L-l}_{\vec{k}+\vec{\xi}}$ with $L-l=0$, the output becomes

$$S_{\vec{k},p_t} = \text{integrated terms} - \sum_{\vec{\xi}\neq\vec{0}\in B_r^2}\frac{a_L(\vec{\xi})S_{\vec{k}+\vec{\xi}}}{A}. \tag{36}$$

This corresponds to the presence of a nonconstant coefficient of the highest power p_t term in the denominator of (10).

A state–space representation can be obtained by assigning a state variable to outputs of each one of the integrators in Fig. 7. The state–space representation is subsequently used to

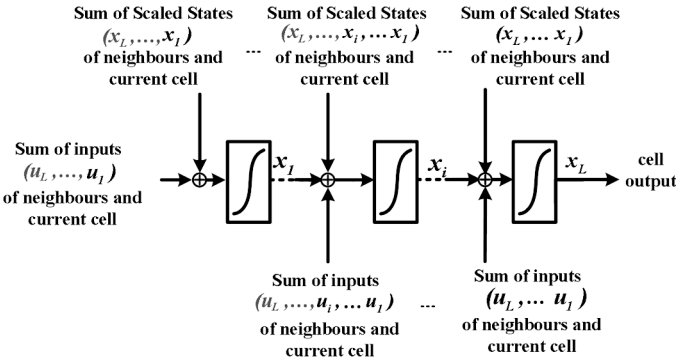


Fig. 8. Schematic of the SFG implementation of MLCNNs [1]with feedforward and feedback interlayer interactions. Symbols $x_1,\ldots x_{L-l},\ldots x_L$ are used to denote the multiple states at a single cell with each integrator implementing a single first-order state-space equation. Note that the coupled states of MLCNNs with feedforward interlayer connections only are expressed as solid text whereas coupled states resulting from interlayer feedforward and feedback MLCNN connections are shown in shaded texts.

synthesize the analog circuit implementation of the network [15]. Equation (36) suggests that the output of the system does not equal to the state but the difference of the state and some "inputs" (outputs of neighboring cells). Bearing in mind that the neighboring output terms $S_{\vec{k}+\vec{\xi}}$ in (36) must also satisfy the same dynamics, (36) has to be satisfied for each network cell. This reveals that extra algebraic constraints are imposed on the outputs of neighboring cells as well as arbitrary input/output coupling, when (36) is required [12]. This feature is also shared by CYCNN [1] structures. At a first glance, the realization of (36) might be problematic due to the algebraic constraints. However, for practical analog VLSI implementations, the extra algebraic constraints are realized in real-time by the physics of circuit components and fundamental electrical laws. Note that the number of integrators required is equal to the maximum degree of p_t in the denominator of the STTF (for STTFs with real coefficients.) It should be clarified that (35) suggests that the derivative diffusion does not require extra differentiators, and by manipulating SFG paths [18](i.e., for a state variable one would require the output of an integrator, whereas for the time-derivative of a state variable one would refer to the input of an integrator immediately before the state variable) one can implement the desired dynamics. For example, in our on-going work on physical network realizations [11], we have adopted a G_m–C implementation where the state derivative at the input of an integrator is "sensed" with a class-AB current mirror which collects and replicates the incoming currents to the integrator.

B. On SFG Relations With the MLCNN

Multilayered CNNs (MLCNNs) have been suggested in the original CNN definition and defined as a state-space (i.e., coupled first-order differential equations) formalism in [1]. This enables a direct translation from state-space to SFG with each first-order equation represented as a single integrator in the SFG (given that we remove the output nonlinearity). The general SFG for a MLCNN cell is shown in Fig. 8. Despite its rich dynamics for system modeling [19], limited research has been carried out in exploiting it for linear spatio-temporal filtering until recently [20]. To contribute to the revelation of the spatio-temporal filtering capability of MLCNNs in the context of STTFs, we consider a two layer *linearized* MLCNN as an example and distinguish between two cases: 1) with feedforward interlayer connections only and 2) with both feedforward and feedback interlayer connections. Fig. 8 illustrates the general SFG for these two cases.

1) Feedforward Inter-Layer Connections Only: The two-layered CNN state-space equations are given by

$$c_1\dot{x}_1(\vec{k}) = -R_1^{-1}x_1(\vec{k}) + I_1 + \sum_{\vec{\xi}\in B_r^2} a_0^{11}(\vec{\xi})x_1(\vec{k}-\vec{\xi}) + \sum_{\vec{\xi}\in B_r^2} b_0^{11}(\vec{\xi})u_1(\vec{k}-\vec{\xi}) \tag{37}$$

$$c_2\dot{x}_2(\vec{k}) = -R_2^{-1}x_2(\vec{k}) + I_2 + \sum_{\vec{\xi}\in B_r^2} a_0^{21}(\vec{\xi})x_1(\vec{k}-\vec{\xi}) + \sum_{\vec{\xi}\in B_r^2} a_0^{22}(\vec{\xi})x_2(\vec{k}-\vec{\xi}) + \sum_{\vec{\xi}\in B_r^2} b_0^{21}(\vec{\xi})u_1(\vec{k}-\vec{\xi}) + \sum_{\vec{\xi}\in B_r^2} b_0^{22}(\vec{\xi})u_2(\vec{k}-\vec{\xi}) \tag{38}$$

where x_1 and x_2 denote the state variable of the first and second layer, respectively, and u_1 and u_2 denote the respective input of the first and second layer. Assuming a single input layer $u_2 = u_1$ with $I_1 = I_2 = 0$ and taking $x_2 = y$ as the output, we can derive the STTF by taking the Laplace and z-transforms of (37) and (38) and eliminating x_1

$$\frac{Y}{U_2} = \frac{P_1(z_x, z_y, p_t)}{Q_1(z_x, z_y, p_t)} \tag{39}$$

with

$$P_1(z_x,z_y,p_t) = \left[A_{21}B_{11} + (B_{22}+A_{21})\left(R_1^{-1}-A_{11}\right)\right] + (B_{22}+A_{21})c_1p_t \tag{40}$$

and

$$Q_1(z_x,z_y,p_t) = c_1c_2p_t^2 + \left[c_2(R_1^{-1}-A_{11}) + c_1(R_2^{-1}-A_{22})\right]p_t + \left(R_2^{-1}-A_{22}\right)\left(R_1^{-1}-A_{11}\right) \tag{41}$$

where A_{11}, A_{22}, A_{21}, B_{11}, and B_{22} are real polynomials of the spatial three-domain variables (z_x, z_y), with coefficients, respectively, determined by template coefficients $a_0^{11}(\vec{\xi})$, $a_0^{22}(\vec{\xi})$, $a_0^{21}(\vec{\xi})$, $b_0^{11}(\vec{\xi})$, and $b_0^{22}(\vec{\xi})$. The above STTF explicitly confirms that MLCNNs with feedforward interlayer connections are indeed suitable for spatio-temporal filtering tasks with higher order (≥ 1) temporal dynamics. Equation (39) is similar to the form of the general STTF of networks with second-order temporal derivative diffusion, which is [from (10)]

$$\frac{Y}{U} = \frac{\sum_{l\in\{1,2\}}\sum_{\vec{\xi}\in B_r^2} b_l'(\vec{\xi}) z_x^{\xi_x} z_y^{\xi_y} p_t^l}{\sum_{l\in\{1,2\}}\sum_{\vec{\xi}\in B_r^2} a_l'(\vec{\xi}) z_x^{\xi_x} z_y^{\xi_y} p_t^l}. \tag{42}$$

However, in order for this two-layer CNN to implement the arbitrary second-order (temporal) STTF realizable by the second-

order temporal derivative diffusion network (42), the following constraints need to be satisfied:

$$\sum_{\vec{\xi}\in B_r^2} a_0'(\vec{\xi}) z_x^{\xi_x} z_y^{\xi_y} = \left(R_2^{-1} - A_{22}\right)\left(R_1^{-1} - A_{11}\right) \tag{43}$$

$$\sum_{\vec{\xi}\in B_r^2} a_1'(\vec{\xi}) z_x^{\xi_x} z_y^{\xi_y} = c_2\left(R_1^{-1} - A_{11}\right) + c_1\left(R_2^{-1} - A_{22}\right) \tag{44}$$

$$\sum_{\vec{\xi}\in B_r^2} a_2'(\vec{\xi}) z_x^{\xi_x} z_y^{\xi_y} = c_2 c_1 \tag{45}$$

$$\sum_{\vec{\xi}\in B_r^2} b_0'(\vec{\xi}) z_x^{\xi_x} z_y^{\xi_y} = A_{21}B_{11} + (B_{22} + A_{21})\left(R_1^{-1} - A_{11}\right) \tag{46}$$

$$\sum_{\vec{\xi}\in B_r^2} b_1'(\vec{\xi}) z_x^{\xi_x} z_y^{\xi_y} = (B_{22} + A_{21})c_1 \tag{47}$$

$$\sum_{\vec{\xi}\in B_r^2} b_2'(\vec{\xi}) z_x^{\xi_x} z_y^{\xi_y} = 0. \tag{48}$$

The relations (43)–(45) and (46)–(48) originated from, respectively, comparing the denominators and numerators of (39) and (42). They suggest limitations on the spatio-temporal filtering function of a two-layer CNN with feedforward interlayer connections only when compared with a second-order temporal derivative diffusion network in the sense that the form of STTFs implementable by this MLCNN is relatively restricted. The non-p_t polynomial in the denominator should be expressed as a factorizable polynomial according to (43) for nonconstants A_{11} and A_{22}. In the case where one of A_{11} or A_{22} is a constant, (43)–(44) suggest that $\sum_{\vec{\xi}\in B_r^2} a_0'(\vec{\xi}) z_x^{\xi_x} z_y^{\xi_y}$ and $\sum_{\vec{\xi}\in B_r^2} a_1'(\vec{\xi}) z_x^{\xi_x} z_y^{\xi_y}$ have to be in the same form.

2) Feedforward and Feedback Inter-Layer Connections: However allowing both feedforward and feedback interlayer coupling on a two-layered CNN, (37) becomes

$$\begin{aligned} c_1\dot{x}_1(\vec{k}) = &- R_1^{-1}x_1(\vec{k}) + I_1 + \sum_{\vec{\xi}\in B_r^2} a_0^{11}(\vec{\xi})x_1(\vec{k}-\vec{\xi}) \\ &+ \sum_{\vec{\xi}\in B_r^2} b_0^{11}(\vec{\xi})u_1(\vec{k}-\vec{\xi}) + \sum_{\vec{\xi}\in B_r^2} a_0^{12}(\vec{\xi})x_2(\vec{k}-\vec{\xi}) \\ &+ \sum_{\vec{\xi}\in B_r^2} b_0^{12}(\vec{\xi})u_2(\vec{k}-\vec{\xi}) \end{aligned} \tag{49}$$

(clearly (38) already incorporates the interlayer feedforward and feedback connections and remains unchanged.) Assuming again a single input layer $u_2 = u_1$ with $I_1 = I_2 = 0$, setting again $x_2 = y$ and taking the Laplace and z-transforms, the following STTF is derived:

$$\frac{Y}{U_2} = \frac{P_2(z_x, z_y, p_t)}{Q_2(z_x, z_y, p_t)} \tag{50}$$

with

$$\begin{aligned} P_2(z_x, z_y, p_t) = &\left[A_{21}(B_{11}+B_{12}) + (B_{22}+A_{21})\left(R_1^{-1} - A_{11}\right)\right] \\ &+ (B_{22} + A_{21})c_1 p_t \end{aligned} \tag{51}$$

and

$$Q_2(z_x, z_y, p_t) = Q_1(z_x, z_y, p_t) - A_{21}A_{12} \tag{52}$$

where A_{12} and B_{12} are real polynomials of the spatial z-domain variables (z_x, z_y) with coefficients, respectively, determined by interlayer feedback coefficients $a_0^{12}(\vec{\xi})$ and $b_0^{12}(\vec{\xi})$. Comparing (50) to (39) and to the relation (42): A_{12} and B_{12} provide extra degrees of freedom such that the constraints (43) and (46) is no longer required. Such a 2-layered CNN is thus capable of implementing general STTFs with the coefficient of the p_t^2 term in the denominator being a constant instead of a bi-variate polynomial of (z_x, x_y) promised by (10). In other words, the STTF implementable by such a 2-layered CNN does not seem to include the subset of STTFs (42) from a second-order temporal-derivative network that requires "algebraic constraint implementation" mentioned at the end of Section IV-A. The STTF of the first example given in the next section is *also* implementable with a two-layer CNN. However, to the best of our knowledge, the specific example has not been reported in the literature to be linked with MLCNN theory. Here, we present an implementation based on temporal derivative diffusion networks.

V. Examples

In this section, we provide two examples of spatio-temporal responses implementable by CNNs with our additional time-derivative diffusion connections. The first one being a neuromorphic STTF derived through analytical modeling of recursive visual cortical neural interactions. We show how our proposed network paradigm can be used to approximate STTFs originated from biological models. Our second example involves the design of a specific high pass 3-D spatio-temporal filter with a cone shaped pass/stopband boundary. In a previous publication [17], we included a first-order velocity selective filter [8], [21] as an example. The authors would like to take the opportunity to point out that the example used in [17] is marginally stable [13].

A. Visual Cortical Receptive Field Modeling

Mineiro and Zipser proposed a second-order (temporal) model for spatio-temporal receptive fields found in the visual cortex in [22]. Their analysis took into account recurrent interactions in the cortex resulting in a recursive filtering structure similar to (10). Their receptive field in the frequency domain is given by

$$\begin{aligned} &H_v(\omega_x, \omega_y) \\ &= \frac{\hat{T}_{\Omega_t}\left[\hat{X}^1_{\omega_x,\omega_y}\left(1 + j\Omega_t - \hat{W}^{22}_{\omega_x,\omega_y}\right) + \hat{W}^{22}_{\omega_x,\omega_y}\hat{X}^2_{\omega_x,\omega_y}\right]}{\hat{W}^{12}_{\omega_x,\omega_y}\hat{W}^{21}_{\omega_x,\omega_y} - \left(1 + j\Omega_t - \hat{W}^{11}_{\omega_x,\omega_y}\right)\left(1 + j\Omega_t - \hat{W}^{22}_{\omega_x,\omega_y}\right)} \end{aligned} \tag{53}$$

where $\hat{T}_{\Omega_t}$ denotes the separable part of the temporal profile of the receptive field, and

$$\hat{W}^{12}_{\omega_x,\omega_y} = \hat{W}^{21}_{\omega_x,\omega_y} = -Be^{\frac{-\sigma_m^2(\omega_x^2+\omega_y^2)}{4\pi}} \tag{54}$$

$$\hat{W}^{11}_{\omega_x,\omega_y} = -j\frac{v_0\tau}{2\pi}(\omega_x + \omega_y)e^{\frac{-\sigma_m^2(\omega_x^2+\omega_y^2)}{4\pi}} = -\hat{W}^{22}_{\omega_x,\omega_y} \tag{55}$$

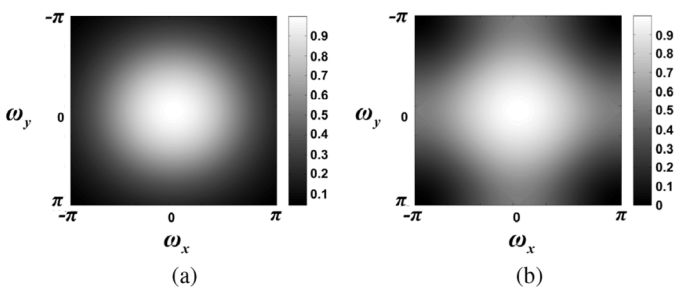


Fig. 9. Gaussian (left) in (54) and its approximation (right) by 2-D cosine functions (58).

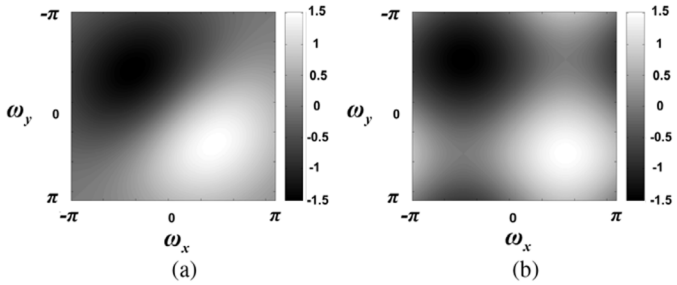


Fig. 10. Gaussian derivative (left) in (55) and its approximation (right) by 2-D sine functions (59).

$$\hat{X}^1_{\omega_x,\omega_y} = \frac{-jC}{2}\left(e^{j\phi}e^{-\frac{\sigma_x^2(\omega_x-\omega_{x0})^2+\sigma_y^2(\omega_y-\omega_{y0})^2}{4\pi^2}} + e^{-j\phi}e^{-\frac{\sigma_x^2(\omega_x+\omega_{x0})^2+\sigma_y^2(\omega_y+\omega_{y0})^2}{4\pi^2}}\right) \tag{56}$$

$$\hat{X}^2_{\omega_x,\omega_y} = \frac{-jC}{2}\left(e^{j\phi}e^{-\frac{\sigma_x^2(\omega_x+\omega_{x0})^2+\sigma_y^2(\omega_y+\omega_{y0})^2}{4\pi^2}} + e^{-j\phi}e^{-\frac{\sigma_x^2(\omega_x-\omega_{x0})^2+\sigma_y^2(\omega_y-\omega_{y0})^2}{4\pi^2}}\right) \tag{57}$$

where B, C, $v_0, \tau, \omega_{x0}, \omega_{y0}, \sigma_m, \sigma_x, \phi$, and σ_y are real constants. Note that the original form of (53) in [22] only has one spatial dimension. To make our discussion here consistent with the analysis presented in Section III, we have extended the STTF from [22] to two spatial dimensions. Equations (56) and (57) are produced by taking the Fourier Transform of a 2-D Gaussian function modulated by 2-D sinusoids with a phase shift of ϕ. As seen from (54)–(57), we have Gaussian, derivative of Gaussian, and Gabor like functions of the spatial frequency variables. In Section III, we have analyzed STTFs in terms of sinusoidal functions of the spatial frequencies. These can be used to approximate (54)–(57). Since we restrict ourselves to filters with real coefficients in this paper, we only consider the denominator of (53) involving spatial terms (54) and (55); but not the Gabor functions (56) and (57) which lead to complex coefficients in the numerator of the STTF. Complex spatio-temporal filtering with two layers of CNN involving our additional time-derivative connections is discussed in a companion paper [12]. For particular parameter values, we can use the following approximation for (54) and (55) in the range of $(\omega_x, \omega_y) \in (-\pi, \pi]x(-\pi, \pi]$

$$\hat{W}^{12}_{\omega_x,\omega_y} = \hat{W}^{21}_{\omega_x,\omega_y} \simeq -\frac{B}{4}[2 + \Gamma_{1,0} + \Gamma_{0,1}] \tag{58}$$

for $\sigma_m = \sqrt{2}$, and

$$\hat{W}^{11}_{\omega_x,\omega_y} = -\hat{W}^{22}_{\omega_x,\omega_y} \simeq -jA(\Delta_{1,0} + \Delta_{0,1}), A = \frac{3.04 v_0 \tau}{2\pi}. \tag{59}$$

The abbreviation of spatial sinusoidal functions in (58) and (59) follows that of (23)–(24). Figs. 9 and 10 compare (54)–(55) and their respective approximation (58)–(59). The denominator of (53) can now be approximated by

$$\frac{B^2}{16}\left(5 + 4\Gamma_{1,0} + 4\Gamma_{0,1} + \Gamma_{1,-1} + \Gamma_{1,1} + \frac{\Gamma_{2,0}}{2} + \frac{\Gamma_{0,2}}{2}\right) - A^2\left(1 - \frac{\Gamma_{2,0}}{2} - \frac{\Gamma_{0,2}}{2} + \Gamma_{1,-1} - \Gamma_{1,1}\right) - 1 + \Omega_t^2 - 2j\Omega_t. \tag{60}$$

Following the analysis presented in Section III, we evaluate the magnitude of (60), with contributions from the real and imaginary parts, respectively, given by

$$R_v = \left[\frac{B^2}{16}\left(5 + 4\Gamma_{1,0} + 4\Gamma_{0,1} + \Gamma_{1,-1} + \Gamma_{1,1} + \frac{\Gamma_{2,0}}{2} + \frac{\Gamma_{0,2}}{2}\right) - A^2\left(1 - \frac{\Gamma_{2,0}}{2} - \frac{\Gamma_{0,2}}{2} + \Gamma_{1,-1} - \Gamma_{1,1}\right) - 1 + \Omega_t^2\right]^2 \tag{61}$$

$$I_v = 4\Omega_t^2. \tag{62}$$

Since both (61) and (62) are even functions of Ω_t, the spatial response will be symmetrical about $\Omega_t = 0$ as Ω_t varies (the visualization is omitted due to a lack of space). This is also true for the original terms (54)–(55). Therefore, we conclude that any velocity selectivity due to spatio-temporal orientation in the frequency domain [23] in (53) is purely due to the numerator terms. As for the STTF, we use the relation

$$z_x^{\xi_x} = e^{j\xi_x\omega_x} \quad \text{and} \quad z_y^{\xi_y} = e^{j\xi_y\omega_y} \tag{63}$$

on the unit circles and Euler's theorem and write (58) and (59) in terms of variables z_x and z_y. The denominator of (53) can be approximated by the frequency response of the following STTF:

$$1 \Big/ \left[\frac{5B^2}{16} - 1 - A^2 + \frac{B^2}{8}(z_x + z_x^{-1} + z_y + z_y^{-1}) + \left(\frac{B^2}{32} - \frac{A^2}{2}\right)\left(z_x z_y + z_x^{-1}z_y^{-1} + z_x z_y^{-1} + z_x^{-1}z_y\right) + \left(\frac{B^2}{64} + \frac{A^2}{2}\right)\left(z_x^2 + z_y^2 + z_x^{-2} + z_y^{-2}\right) - 2p_t - p_t^2\right]. \tag{64}$$

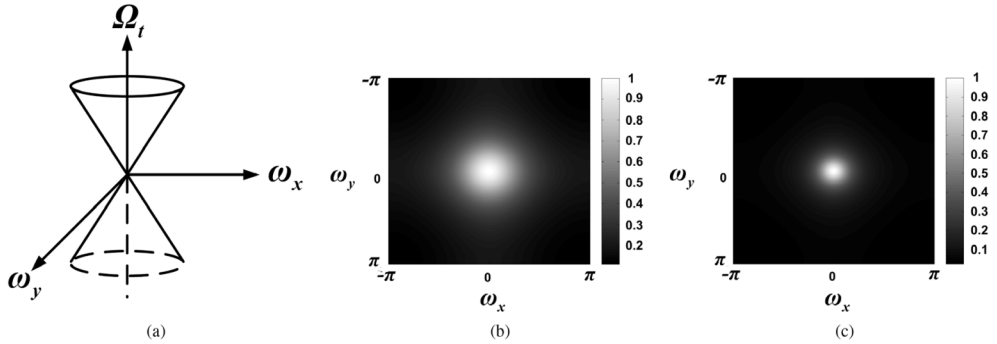


Fig. 11. (a) Ideal cone filter response. The amplitude of the magnitude response equals to unity inside the cones and zero outside. (b) Amplitude response of (65) with $a_c = 1$. (c) Amplitude response of (65) with $a_c = 5$.

This corresponds to a network with first and second-order temporal derivative diffusion to ground.

B. Spatio-Temporal Cone Filter

In this example, we apply the empirical method presented in Section III to design a spatio-temporal "Cone" filter. We start with a two dimensional spatial filter and by transforming its coefficients into temporal frequency-dependent terms, a temporal frequency-dependent spatial filter is created. Cone filters are three dimensional high pass filters with their passband and stopband separated by two tip-to-tip cones. An ideal cone response is illustrated in Fig. 11(a). Due to the high computational cost of implementing three dimensional convolutions, recursive cone filter approximation have drawn considerable attention from the research community [8], [24]–[26]. Here we show how approximate cone-like responses can be produced by CNNs with our additional time-derivative diffusion connections. Consider a two-dimensional CNN filter [2] with 2-D z-domain transfer function

$$H_L(z_x, z_y) = \frac{1}{1 + 4a_c - a_c\left(z_x^{+1} + z_x^{-1} + z_y^{+1} + z_y^{-1}\right)} \tag{65}$$

and frequency response given by

$$H_L(\omega_x, \omega_y) = \frac{1}{1 + 2a_c(1 - \cos\omega_x) + 2a_c(1 - \cos\omega_y)}. \tag{66}$$

The magnitude response of (66) as parameter $a_c \in R$ is varied is presented in Fig. 11(b)–(c). Two things can be noticed. First, the pass and stop band boundary (for simplicity, we thereafter refer to this as the "passband boundary") is approximately circular. Secondly, the passband boundary decreases in "radius" as a_c increases. Observe the ideal spatio-temporal cone characteristic in Fig. 11(a) and assume a slice parallel to the (ω_x, ω_y) axis: the passband boundary is circular. As we move along the Ω_t axis, the boundary increases in radius with the absolute value of Ω_t. Therefore, we aim to express a_c in (66) as a function of Ω_t such that an increase in $|\Omega_t|$ causes a decrease in a_c and hence an increase in radius of the passband boundary of the spatial filter (65). In this way, the desired temporal frequency-dependent spatial filter response can be synthesized. A natural choice is

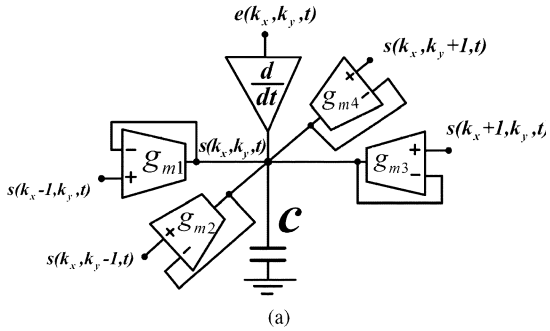


Fig. 12. Network for cone filter approximation.

$$a_c = \frac{a_c'}{p_t} = \frac{a_c'}{j\Omega_t}. \tag{67}$$

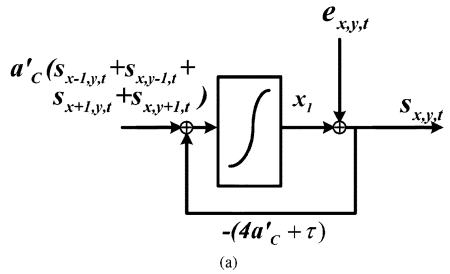
Substituting (67) in (65) and rearranging, we have

$$H_L'(z_x, z_y) = \frac{p_t}{p_t + 4a_c' - a_c'\left(z_x^{+1} + z_x^{-1} + z_y^{+1} + z_y^{-1}\right)}. \tag{68}$$

To ensure filter stability [7], [13], we introduce an extra constant term τ_c in the denominator

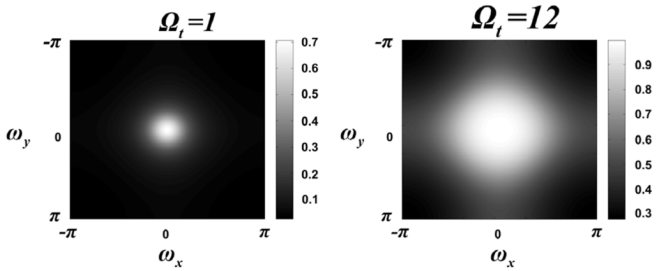
$$H_L'(z_x, z_y) = \frac{p_t}{p_t + 4a_c' - a_c'\left(z_x^{+1} + z_x^{-1} + z_y^{+1} + z_y^{-1}\right) + \tau_c}. \tag{69}$$

The corresponding network and SFG is shown in Figs. 12 and 13, respectively. As seen in Fig. 12, a temporal derivative diffusion from the input node is needed. The response of (69) as we move along the Ω_t axis is shown in Fig. 14, with an approximately "cone" characteristic (since the amplitude response is an even function of Ω_t, we only show responses for positive Ω_t values.) Therefore, by introducing the appropriate temporal derivative connections and utilizing the concept of temporal frequency-dependent spatial filters, we tailor the desired temporal characteristics upon a spatial filter (65) and



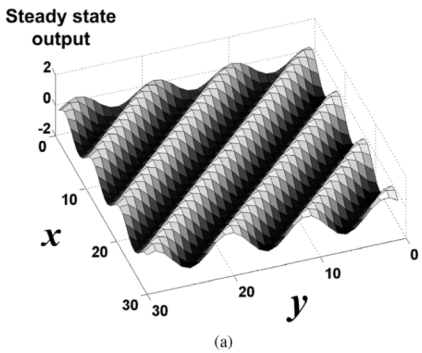
(a)

Fig. 13. SFG for the implementation of a cone filtering network.



(a) (b)

Fig. 14. Two magnitude response "slices" parallel to the $\Omega_t = 0$ plane of a cone approximation implemented with a CNN with temporal derivative diffusion. Further slices with different Ω_t values are omitted due to a lack of space.

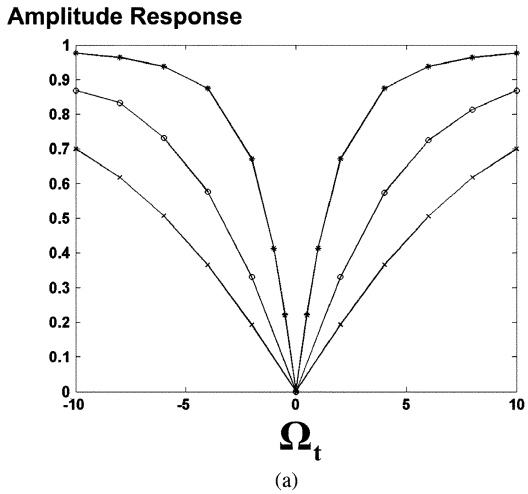


(a)

Fig. 15. Steady-state output snapshot at a particular time instance (after temporal transient had died down) when an input at frequency $(\omega_x, \omega_y, \Omega_t) = (0.7, 0.7, 10)$ is applied to the cone filtering network.

managed to create a cone filter approximation. Note that (69) can be re-expressed as the sum of a constant term and a linear CNN STTF with a nonconstant numerator independent of p_t. This suggests an alternative implementation of the cone approximation based on linear CNNs and some post processing (which has not been reported elsewhere in CNN literature). However, the network based on temporal derivative diffusion provides a simpler approach with only a single numerator term corresponding to a single element in the input time-derivative template.

Simulation results are shown in Figs. 15–17. Spatio-temporal sinusoidal signals with varying spatial and temporal frequencies are applied to a 30×30 network and the steady-state output is presented in Figs. 16 and 17. Fig. 15 shows a typical output at



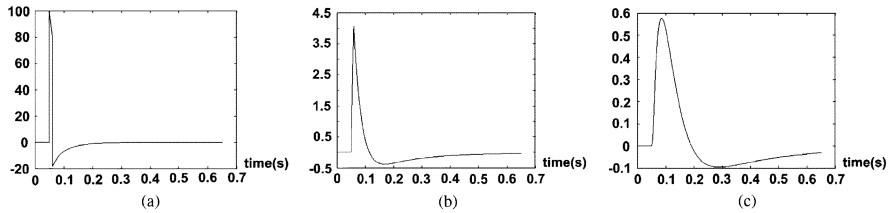
(a)

Fig. 16. Simulation results for a 30×30 network approximating the cone response. Spatio-temporal sine waves of different spatial and temporal frequencies are applied to the network and the output is observed for each input spatio-temporal sine waves. The vertical axis shows the output sinusoidal amplitude of the middle pixel at location (15, 15). The horizontal axis shows the temporal frequency of input. Results for three input spatial frequencies are shown. Symbols $(*, o, x)$ are for spatial frequencies $(\omega_x, \omega_y) = (0.35, -0.35), (0.7, 0.7)$ and $(-1, -1)$, respectively.

a particular time instant. Fig. 16 shows the magnitude of the output spatio-temporal sine wave when we vary the temporal frequency of the input while the spatial frequency is fixed at three different points. As we move away from the frequency-domain origin by varying the spatial frequency from $(0.35, -0.35)$ to $(-1, -1)$, we observe that an input of higher temporal frequency is required to give the same output level as inputs with lower spatial frequencies. This confirms a cone filtering characteristic. Fig. 17 shows the output signal at various spatial locations when a pulse of height 100 (relative units) and width of 0.01 seconds is applied at cell (15, 15) of the 30×30 network, the spatio-temporal output thus approximates the impulse response of our cone filter. As seen from Fig. 17, the response drops quickly across time in center cell (15, 15) (where the "impulse" is applied) and the output amplitude decays abruptly across space. This suggests the "preferred input" of the network is a fast flashing dot occupying a small space, which confirms the high pass characteristic of the filter. Furthermore, note the temporal characteristic (time constant) changes across space from Fig. 17(a) to (c). i.e., the response takes a longer time to decay in Fig. 17(c) than it took in Fig. 17(a). This confirms the space-time nonseparable characteristic of our cone filtering network.

VI. Conclusion

A new modified general form of linear CNNs targeting spatio-temporal filtering applications is introduced by incorporating novel temporal derivative "diffusion" between neighboring CNN cells. This results in a convenient one to one relationship of 3-D rational STTF terms with network connections. It is hoped that this paper serves as a useful introduction to CNNs with additional temporal derivative diffusion



(a) (b) (c)

Fig. 17. Simulated impulse response of a cone filtering network. (a) Output signal at spatial location (15, 15) when an impulse is applied to a 30×30 cone network at location (15, 15). (b) Identical output signals observed at spatial locations (15, 16), (16, 15), (15, 14), and (14, 15) when an impulse is applied to a 30×30 cone network at location (15, 15). (c) Identical output signals observed at spatial locations (14, 16), (16, 16), (16, 14), and (14, 14) when an impulse is applied to a 30×30 cone network at location (15, 15).

connections and provides extra insight in mixed-domain STTFs that are realizable with such network topologies.

ACKNOWLEDGMENT

The authors would like to thank the anonymous reviewers for their feedback which improved the clarity of this manuscript.

REFERENCES

[1] L. O. Chua and L. Yang, "Cellular neural networks: Theory and applications," *IEEE Trans. Circuits Syst. I, Fundam. Theory Appl.*, vol. 35, pp. 1257–1290, Oct. 1988.

[2] B. E. Shi and L. O. Chua, "Resistive grid image filtering: An input/output analysis via the cnn framework," *IEEE Trans. Circuits Syst. I, Fundam. Theory Appl.*, vol. 39, no. 7, pp. 531–548, Jul. 1992.

[3] K. Crounse, C. Wee, and L. O. Chua, "Methods for image processing and pattern formation in cellular neural networks: A tutorial," *IEEE Trans. Circuits Syst. I, Fundam. Theory Appl.*, vol. 42, no. 11, pp. 583–601, Oct. 1995.

[4] B. E. Shi, "2-D focal plane steerable and scalable cortical filters," in *Proc. IEEE Microelectron. Neural, Fuzzy and Bio-Inspired Systems 1999 (MicroNeuro'99)*, 1999, pp. 232–239.

[5] A. B. Torralba and J. Herault, "An efficient neuromorphic analog network for motion estimation," *IEEE Trans. Circuits Syst. I, Fundam. Theory Appl.*, vol. 46, no. 3, pp. 269–280, Mar. 1999.

[6] B. E. Shi and K. Boahen, "Competitively coupled orientation selective cellular neural networks," *IEEE Trans. Circuits Syst. I, Fundam. Theory Appl.*, vol. 49, no. 3, pp. 388–394, Mar. 2002.

[7] B. E. Shi, T. Roska, and L. O. Chua, "Design of linear cellular neural networks for motion sensitive filtering," *IEEE Trans. Circuits Syst. II, Analog Digit. Signal Process.*, vol. 40, no. 5, pp. 320–331, May 1993.

[8] Y. Zhang and L. T. Bruton, "Applications of 3-d lcr networks in the design of 3-d recursive filters for processing image sequences," *IEEE Trans. Circuits Syst. Video Technol.*, vol. 4, no. 4, pp. 369–382, Aug. 1994.

[9] H. E. Mutluay and M. M. Fahmy, "Analysis of n-d general-support filters," *IEEE Trans. Acoust., Speech, Signal Process.*, vol. 33, no. 4, pp. 972–982, 1985.

[10] R. C. Galan, F. Jimenez-Garrido, R. Dominguez-Castro, S. Espejo, T. Roska, C. Rekeczky, T. Petras, and A. Rodriguez-Vasquez, "A bio-inspired two-layer mixed-signal flexible programmable chip for early vision," *IEEE Trans. Neural Netw.*, vol. 14, no. 5, pp. 1313–1336, Nov. 2003.

[11] H. M. D. Ip, E. M. Drakakis, and A. A. Bharath, "Towards analog vlsi arays for nonseparable 3-D spatiotemporal filtering," in *Proc. IEEE Int. Workshop Cellular Neural Networks Its Applications (CNNA'06)*, Istanbul, Turkey, 2006, pp. 1–6.

[12] H. M. D. Ip, E. M. Drakakis, and A. A. Bharath, "Synthesis of nonseparable 3-D spatiotemporal bandpass filters on analog networks," *IEEE Trans. Circuits Syst. I, Reg. Papers*, vol. 55, no. 2, pp. 286–298, Feb. 2008.

[13] J. H. Justice and J. L. Shanks, "Stability criterion for n-dimensional digital filters," *IEEE Trans. Automat. Contr.*, vol. 18, pp. 284–286, 1973.

[14] G. H. Granlund and H. K. , Eds., *Signal Processing for Computer Vision*. Norwell, MA: Kluwer Academic, 1995.

[15] D. Johns and K. Martin, *Analog Intergrated Circuits Design*. New York: Wiley, 1996.

[16] L. P. Huesman, *Active and Passive Analog Filter Design, an Introduction*. New York: McGraw-Hill, 1993.

[17] H. M. D. Ip, E. M. Drakakis, and A. A. Bharath, "Analog networks for mixed-domain spatiotemporal filtering," in *Proc. IEEE Int. Symp. Circuits Syst. (ISCAS'05)*, Kobe, Japan, May 2005, vol. 14, pp. 3918–3921.

[18] W. K. C. , Ed., *The Circuits and Filters Handbook*. : CRC and IEEE Press, 1995.

[19] D. Balya, I. Petras, T. Roska, R. Carmona, and A. Rodriguez-Vasquez, "Implementing the multilayer retinal model on the complex-cell cnn-um chip prototype," *Int. J. Bifurc. Chaos*, vol. 14, no. 2, pp. 427–451, 2004.

[20] B. Shi, "An eight layer cellular neural network for spatio-temporal image filtering," *Int. J. Circuit Theory Appl.*, vol. 34, pp. 141–164, 2006.

[21] R. K. Bertschomann, N. R. Bertley, and L. T. Bruton, "A 3-d integrator-differentiator double-loop (idd) filter for raster-scan video processing," in *Proc. IEEE Int. Symp. Circuits Syst. (ISCAS'95)*, 1995, vol. 1, pp. 470–473.

[22] P. Mineiro and D. Zipser, "Analysis of direction selectivity arising from recurrent cortical interactions," *Neural Comput.*, vol. 10, pp. 353–371, 1998.

[23] B. Jahne, H. HauBecker, and P. G. , Eds., *Handbook of Computer Vision and Application, Volume 2: Signal Processing and Pattern Recognition*. New York: Academic, 1999.

[24] H. E. Mutluay and M. M. Fahmy, "Frequency-domain design of n-d digital filters," *IEEE Trans. Circuits Syst.*, vol. CAS-32, no. 12, pp. 1226–1233, Dec. 1985.

[25] J. K. Pitas and A. N. Venetsanopoulos, "The use of symmetries in the design of multidimensional digital filters," *IEEE Trans. Circuits Syst.*, vol. CAS-33, no. 9, pp. 866–873, Sep. 1986.

[26] M. Bolle, "A closed form design method for recursive 3-D cone filters," in *Proc. IEEE Int. Symp. Acoust. Speech, Signal Process.*, 1994, vol. VI, pp. 19–22.



Henry Man D. Ip (M'07) was born in England in 1980. He received the M.Eng. degree in information systems engineering (first class), jointly from the Department of Electrical and Electronics Engineering and the Department of Computing, Imperial College London, London, U.K., in 2003. Since then, he has been working toward the Ph.D. degree in bioengineering at the same college.

His thesis involves the theory and analog VLSI implementations of linear cellular neural networks for spatial and spatio-temporal filtering.



Emmanuel M. Drakakis (M'05) received the B.Sc. degree in physics and the M.Phil. degree in electronic physics and radioelectrology from Aristotle University of Thessaloniki, Macedonia, Greece, in 1991 and 1994, respectively, and the Ph.D. degree in analogue IC design from the Department of Electrical And Electronic Engineering, Imperial College London, London, U.K., in 1999.

He is currently a Senior Lecturer in the Department of Bioengineering at Imperial where he joined in October 2001 and founded the "Bioinspired VLSI Circuits and Systems Group." The Group's research focuses on circuits and systems "for and from biology." He has also authored and co-authored more than 50 peer-reviewed publications.

Dr. Drakakis has been awarded a prize by the Hellenic Army's Research and Technology Center (1995) whereas between 1996–1998 he was sponsored by the Micro-Electronics Research Center (MERC) of LM Ericsson-Krista—Stockholm. In 2006, he received the Rector's Award for Research at Imperial. He is a member of the IEEE BIOCAS and CNNA technical committees, is past Associate Editor of IEEE TRANSACTIONS ON CIRCUIT AND SYSTEMS—I: REGULAR PAPERS and IEEE TRANSACTIONS ON CIRCUIT AND SYSTEMS—II: EXPRESS BRIEFS, past Guest Assistant Editor for *IEE Electronics Letters* and past Subject Editor for the *International Journal of Electronics*.



Anil Anthony Bharath (M'98) received the B.Eng. degree with first-class honours from the Department of Electronic and Electrical Engineering, University College London, London, U.K., in 1988, and the Ph.D. degree from the Department of Electrical and Electronic Engineering, Imperial College London, London, U.K., in 1993.

Since 1991, he has held the post of Lecturer, then Senior Lecturer in Medical Imaging in the Department of Bioengineering at Imperial College London. In 2005, he was appointed to the post of Reader in Image Analysis. From October to December 2006, he was visiting academic at the Signal Processing Group, Department of Engineering, University of Cambridge, Cambridge U.K. He has worked and published in the areas of medical image analysis, computer vision and signal processing, and has worked as consultant to the imaging sciences industry, primarily in the fields of medical imaging and medical informatics. His current research interests are in visual pattern recognition, signal and image representations, statistical signal models, and biological vision.

Dr. Bharath jointly presented the 2003 Rosen Lecture at the Royal Institution on Art and Imaging with the visual artist D. Fern.